Model-Based Bootstrapping on Classified Tensor Morphologies using Constrained Two-Tensor Model

Abstract. In this study, fast and clinically feasible model-based bootstrapping algorithms using a geometrically constrained two-tensor diffusion model are employed for estimating uncertainty in fibre-orientation. Voxels are classified based on tensor morphologies before applying single or two-tensor model-based bootstrapping algorithms. Classification of tensor morphologies allows the tensor morphology to be considered when selecting the most appropriate bootstrap procedure. A constrained two-tensor model approach can greatly reduce data acquisition times and computational time for whole bootstrap data volume generation compared to other multi-fibre model techniques, facilitating widespread clinical use. For comparison, we propose a new repetition-bootstrap algorithm based on classified voxels and the constrained two-tensor model. White matter tractography with these bootstrapping algorithms is also developed to estimate the connection probabilities between brain regions, especially regions with complex fibre configurations. Experimental results on a hardware phantom and human brain data demonstrate the superior performance of our algorithms compared to conventional approaches.

1 Introduction

Bootstrapping of repeated diffusion weighted MRI data sets allows non-parametric estimation of uncertainty in the inferred fibre orientation [1]. Model-based bootstrap methods (wild bootstrapping [2] and residual bootstrapping [3]) using a single-data set have been presented as an alternative to repetition bootstrapping. Generally, the single diffusion tensor model does not correctly express the microstructure in voxels that contain more than one fibre orientation. Model-based and repetition-bootstrapping fibre tracking methods using DTI can fail when fibre tracts pass through voxels containing complex configurations [4]. These configurations are characterised by disk-shaped (planar) forms of the tensor. The development of new models based on HARDI seeks to provide solutions to this problem [5-8]. HARDI-based methods, including multi-tensor models [5] and Q-ball imaging [6], require longer acquisition times than conventional DTI and are generally not suitable for clinical applications. The high b values utilised in some cases increase sensitivity to subject motion, which is also undesirable for a clinical setting. Constrained spherical deconvolution [7] has shown good results when applied to relatively low angular resolution DW data, however, only orientational information can be obtained with this method. To solve some of the above problems, a geometrically constrained two-tensor model for resolving fibre crossings was introduced in [8].

More than a third of voxels in human white matter contain crossing fibre bundles at the current resolution of DWMRI, and these voxels challenge statistical models for tensor estimation and fibre tracking. Therefore, developing a proper bootstrap method for estimating fibre orientation in these voxels is important. Yuan et al. [4] showed that repetition and wild bootstrapping may fail to quantify the uncertainties in DTI derived parameters in oblate voxels. Therefore, to use bootstrap methods correctly, the morphology of a tensor must be known. The validity of model-based

bootstrapping strongly depends on the correct specification of the fitted model used to estimate tensors. This raises concerns about the validity of bootstrapping those fibre pathways that pass through voxels which containing different tensor morphologies. Our solution is to classify tensor morphologies before the application of bootstrap algorithms, which allows the use of appropriate tensor morphologies.

In this work, fast and clinically feasible wild and residual bootstrapping algorithms for estimating uncertainty in fibre-orientation are presented based on a geometrically constrained two-tensor diffusion model. Voxels are classified based on tensor morphologies before applying single or two-tensor model-based bootstrapping algorithms. Probabilistic fibre tractography with these bootstrapping algorithms is also developed to estimate connection probabilities between brain regions, especially regions with complex fibre configurations. We evaluate the tracking algorithm quantitatively using a hardware phantom and human *in vivo* data. For comparison, a new constrained two-tensor repetition bootstrapping algorithm is developed based on the same morphology classification approach as used for model-based bootstrapping.

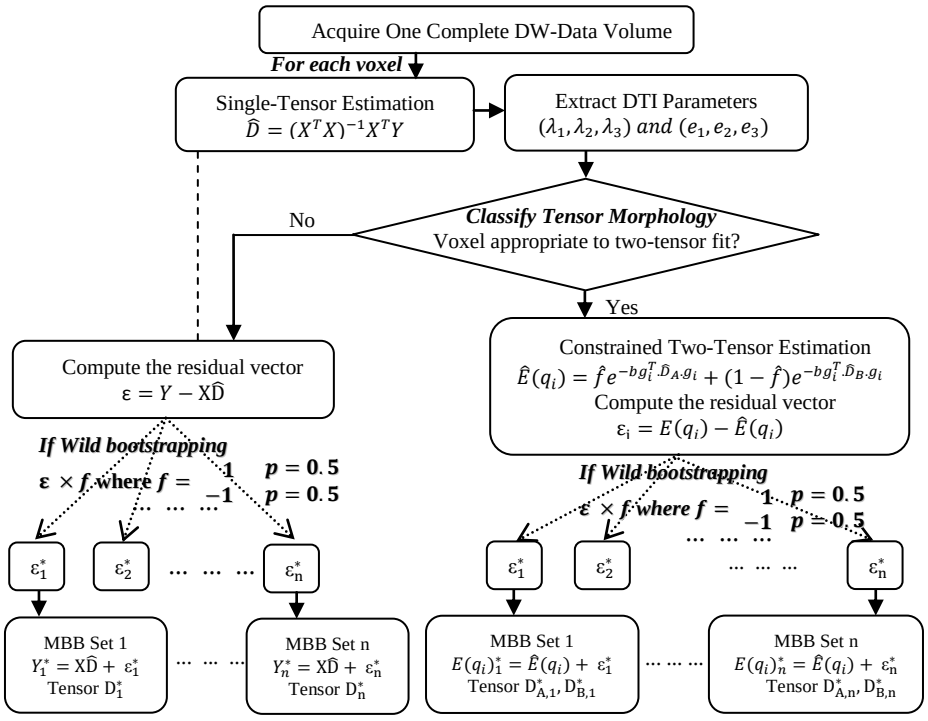

Fig. 1. Two-tensor model-based bootstrap algorithms on classified tensor morphologies.

2 Two-Tensor Model-Based Bootstrapping Algorithms

The two-tensor model-based algorithms used in this study are illustrated by Fig.1. The detail of the individual steps are as follows.

Step 1- Data Acquisition and Initial Tensor Fitting. Intensities of the measured diffusion-weighted signals are quantified for a single-tensor model by:

$$S_i = S_0 e^{-b g_i^T . D . g_i}, \quad i = 1, 2, \ldots, N \tag{1}$$

where S_i and S_0 are the signal intensities with and without diffusion weighting, b is the diffusion weighting factor, g the unit vector of the gradient direction, N the total number of experiments and D the diffusion tensor. Applying a log-transformation to Eq(1), the estimation of D becomes a well-known multiple linear regression form:

$$Y_i = (XD)_i + \varepsilon_i \qquad i = 1, 2, \ldots, N \tag{2}$$

where X is a design matrix of different diffusion gradient directions, $(XD)_i$ is the product of the i^{th} row of X and D, and ε_i is a random sample from the residuals of the original regression model. To estimate the tensor D, Eq (1) is solved by the following linear least squares (LLS) method.

$$\widehat{D} = (X^T X)^{-1} X^T Y \tag{3}$$

The residuals from the LLS fit used to generate the model based bootstrap (MBB) samples in Step 4 are calculated from $\varepsilon = Y - X\widehat{D}$ (4)

Step 2- Classifying Tensor Morphology. The three types of degenerate tensors are isotropic (λ_1=λ_2=$\lambda_3 > 0$), oblate ($\lambda_1 = \lambda_2 > \lambda_3 > 0$), or prolate ($\lambda_1 > \lambda_2 = \lambda_3 > 0$) where λ_i (i =1,2,3) are the three eigenvalues of the tensor $\widehat{D}$. To classify tensor morphologies (TM), we developed an algorithm based on three equalities described by Zhu et al. [9], where the algorithm sequentially checks whether each voxel in the image is isotropic (I), oblate (O), or prolate (P). This classifying algorithm uses a threshold α_i (i=1-4), as described below.

For each voxel { IF $|\lambda_1 - \lambda_3| < \alpha_1$ THEN TM = I
ELSE IF $|\lambda_1 - \lambda_2| < \alpha_2$
THEN IF $|\lambda_2 - \lambda_3| < \alpha_3$ THEN TM = I
ELSE TM = O
ELSE IF $|\lambda_2 - \lambda_3| < \alpha_4$ THEN TM = P
ELSE TM = I }

We use three invariants to characterise the shape of the tensor ellipsoids proposed by Westin et al. [10] to compare our classification algorithm. Westin et al. [10] defined three measures which describe how similar the diffusion ellipsoid is to the linear (cl); planar (cp); and spherical (cs) case respectively. Two-tensor model-based algorithms were applied to oblate (TM=O) voxels and single-tensor model-based algorithms to the other voxels, because only planar voxels are amenable to two-tensor fitting.

Step 3- Constrained Two-Tensor Model Estimation. A geometrically constrained two-tensor model [8] was used to find the two diffusion tensors and reduce the number of degrees of freedom in the original multi-tensor model [5].

$$S_i = S_0 f e^{-b g_i^T . D_A . g_i} + S_0 (1 - f) e^{-b g_i^T . D_B . g_i} \quad i = 1, 2, \ldots, N \tag{5}$$

where D_A and D_B represent the tensor from each compartment, and f and $(1 - f)$ are the signal fractions from D_A and D_B. This model assumes that both fibre tracts are constrained in the plane spanned by the first two eigenvectors $e_1$and e_2 from the single-tensor fit. Given the above constraint, two tensors D_A and D_B are described as

$$D_A = \begin{bmatrix} d_{a1} & d_{a3} & 0 \\ d_{a3} & d_{a2} & 0 \\ 0 & 0 & \lambda_3 \end{bmatrix}, D_B = \begin{bmatrix} d_{b1} & d_{b3} & 0 \\ d_{b3} & d_{b2} & 0 \\ 0 & 0 & \lambda_3 \end{bmatrix}$$

where $d_{p1} = \cos^2\phi_p \lambda_1 + \sin^2\phi_p \lambda_3$, $p \epsilon \{a, b\}$

$d_{p2} = \sin^2\phi_p \lambda_1 + \cos^2\phi_p \lambda_3$ and $d_{p3} = \cos\phi_p \sin\phi_p \, (\lambda_1 - \lambda_3)$

With the single-tensor fit determining the orientation of e_3 and the minor eigenvalue λ_3, the remaining free parameters are ϕ_a and ϕ_b , the angles subtended in the plane by the two principal directions and λ_1 is the principal diffusivity which is assumed to be same for both fibre tracts. The gradient vectors are transformed into a 2-D coordinate system; $g \rightarrow \tilde{g}$.

$$E(q_i) = \frac{S_i}{S_0} = fe^{-b\tilde{g}_i^T.D_A.\tilde{g}_i} + (1-f)e^{-b\tilde{g}_i^T.D_B.\tilde{g}_i} \quad (6)$$

The equation becomes a system of non-linear equations and minimises to

$$\sum_i (\hat{E}(q_i) - E(q_i))^2,$$

which gives the estimated tensor elements $\hat{D}_A$, $\hat{D}_B$ and the fraction $\hat{f}$. The Levenberg-Marquardt optimisation algorithm is used to estimate non-linear equations. In each gradient direction $i (i = 1 \ldots N)$, a residual ε_i is calculated according to

$$\varepsilon_i = E(q_i) - \hat{E}(q_i) \quad (7)$$

Step 4- Model-based Bootstrap Sample Generation. The residual vector ε from the single-tensor fit (Eq(4)) or two-tensor fit (Eq(7)) is used to generate the MBB samples. In order to resample the errors, the wild bootstrapping approach assumes symmetry in the distribution of residuals for a given data point, and a residual value, ε_j^*, was randomly chosen and multiplied by -1 or 1(p=0.5) with replacement from the set of all residuals ε. The residual bootstrapping approach assumes that all residuals have similar distributions and a residual value ε_j^* randomly chosen among the set of all residuals ε. Model-based resampling is then performed to construct many data sets, Y^* or $E(q_i)^*$:

$Y_j^* = X\hat{D} + \varepsilon_j^*$ for voxels with single tensor.

$E(q_i)_j^* = \hat{E}(q_i) + \varepsilon_j^*$ for voxels with two tensors.

Resampling $\varepsilon^* = [\varepsilon_1^*, \varepsilon_2^*, \ldots, \varepsilon_N^*]$ and estimating D^* or D_A^* and D_B^* from Y^* or $E(q_i)^*$ are repeated for some fixed large number n to acquire n independent MBB samples.

Step 5- Probabilistic Fibre Tractography. Having generated n tensor volumes, a 4th order Runge-Kutta streamline tracking algorithm was used to propagate streamlines bidirectionally from seed points. The algorithm was repeated for n volumes to generate n tracts for each seed point. Every voxel in a volume contains either 1 (single tensor) or 2 principal eigenvectors (two tensors) as appropriate for the tensor morphology of the particular voxel. If the seed point voxel has two tensors then two separate trajectories are generated from the seed point using two fibre orientations. The deterministic tracking algorithm then propagates the trajectories to the next position. If the next position contains two fibre orientations, the two principal eigenvectors are compared to determine which if either of the trajectories should be followed. We choose the fibre orientation which has the smallest angular difference to the principal eigenvector calculated from the previous position.

3 Methodology

Phantom Data: 3T DW-data were acquired from a physical phantom (http://www.lnao.fr/spip.php?article106) with 3x3x3 mm^3 voxel resolution, b =1500 s/mm^2 and 64 diffusion directions.

***In Vivo* Data:** 3T DTI data were obtained on a healthy volunteer with 2x2x2 mm^3 voxel resolution using 32 diffusion-encoding gradient directions and b = 1300 s/mm^2. The acquisition was repeated 8 times for repetition-bootstrap analysis. The diffusion-weighted images were first corrected for bulk motion and eddy current distortions.

Two-Tensor Model-based Bootstrapping: We applied the model-based bootstrap algorithms, to the phantom data and the first of the eight repeated *in vivo* diffusion-weighted datasets, described above, and generated 1000 MBB volumes. The voxels were classified based on the classification algorithm before applying single-tensor and two-tensor model-based bootstrapping algorithms. The probabilistic tractography was then applied to the MBB volumes of phantom-data from 4 pre-defined seed positions; the actual fibre structure from the seed position passing through the different complex fibre configurations as illustrated in Fig. 2. Fibre tracks were generated from user-defined regions in *in vivo* data based on prior anatomical knowledge to delineate the corpus callosum (CC), superior longitudinal fasciculus (SLF) and corticospinal tract (CST). A comparison of the results of our method with that of the single-tensor residual and wild bootstrapping methods applied using the same starting points to extract the same fibre structures in the phantom and *in vivo* are presented.

Performance Analysis: The phantom data was used to test the performance of the single and two-tensor model-based bootstrap probabilistic tracking algorithms. Performance measures were calculated as the error (ξ) in tract estimation, which is a function of distance d from the seed point. The distance d_i at point(x_i, y_i, z_i), is the cumulative total of all Euclidian distances of neighbouring points along the curve up to the (x_i, y_i, z_i) from the seed point. The positive and negative distances are defined by the two directions of the curve from a seed point (Fig. 2). The error ξ_i at distance d_i is defined as the Euclidian distance between the ground-truth curve point at d_i and the resultant curve point at d_i from the seed point. The overall range of d is defined as the maximum d at both ends of the ground-truth curve. The ground truth curves and the curves of the four probabilistic methods, described above, from the 4 seed points of the phantom data were assessed. From the 1000 probabilistic curves, average error values were computed for each method and for each seed point at 10 mm distances.

Two-Tensor Repetition Bootstrapping: Repetition bootstrap methods were used to randomly generate samples for every voxel in each diffusion-encoded image of the *in vivo* data. In each iteration 5 samples were randomly sampled with replacement from the 8 data acquisitions. The signal for each voxel was calculated as the average of the 5 selected samples. This procedure was repeated for each voxel and diffusion-encoded dataset. The resulting data is one volume bootstrap sample. Single or constrained two-tensor models according to the morphology of the voxels, were fitted to the bootstrap data to estimate diffusion tensors for each voxel. A complete bootstrap tractography dataset was obtained by iteratively running the random sampling method 1000 times to generate multiple volume bootstrap data. Fibre tracts were generated using the same region and tracking threshold as the model-based bootstrap tracking.

4 Results and Discussion

Phantom Data: Fig. 2 shows the ground truth of the phantom, complex regions and Westin measures and our classification algorithm results. There was no major difference between the two methods except our algorithms ($\alpha_i = 14 \times 10^{-8}$) identified more isotropic and planar voxels in the expected regions. Tracking results in the phantom data (Fig. 3) show performance differences in the bootstrap tractography

methods. The results of two-tensor model-based tracking are consistent with the ground truth and are able to solve the complex configurations and track properly. In Fig. 3A, ideally, one would expect the tractography trajectories starting from the seed point to cross regions 1 and 3; instead as they enter the fibre crossing region the fibre tracts diverge in the wrong direction. But Fig. 3A (d) shows that the trajectories correctly cross the region and tracts are similar to the expected ground truth. In Fig. 3B, the seed point selected as a target shows the branching ability of the two-tensor model-based bootstrapping algorithm. The estimated pathways of single-tensor model-based bootstrapping (Fig. 3B(c)) have leaked and are dispersed, which makes the main pathway of connectivity more difficult to comprehend. Fig. 3C(d) and Fig. 3D(d) illustrate the connection probability map resulting from probabilistic tractography using two-tensor residual bootstrap tractography. The tractography correctly follows the fibre direction through the fibre-crossing regions: Region 1(Fig. 3C(d)) and Region 2 (Fig. 3D(d)), but not for the results of single-tensor residual bootstrap tractography.

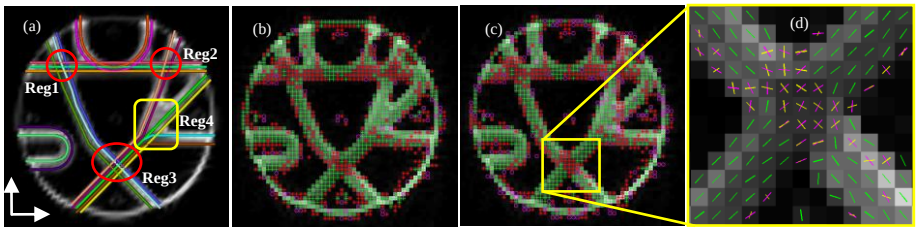

Fig. 2. (a) Ground truth and selected crossing regions (in red circles) and a branching region (in yellow rectangle) (b) Classification using Westin measures (linear (+), planar(*) or spherical (o) shape) and (c) Classification algorithm (d) Constrained two-tensor model estimation.

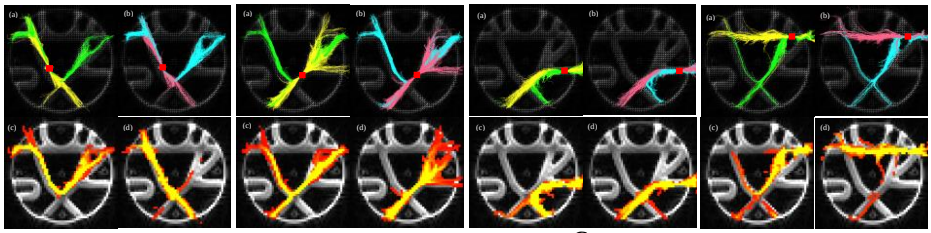

Fig. 3. Tracking results from 4 seed points (seed points are illustrated in the red square) A, B, C and D. (a) Residual bootstrap results: Single-tensor (green) and Two-tensor (yellow) (b) Wild bootstrap results: Single-tensor (blue) and Two-tensor (salmon) (c) Probability map of single-tensor residual bootstrapping (d) Probability map of two-tensor residual bootstrapping.

Performance Analysis: Considering the plots of average error at different distances from the 4 seed points (Fig. 4), generally, the error increases with the distance from the seed point for all four methods. There is not a large difference between the residual and wild bootstrap tracking methods for either the single or two-tensor cases and it is difficult to claim that a particular method generates a higher or lower error. However, the residual bootstrap is generally consistently better than the wild bootstrap, especially in complex regions. Fig 4 shows that single-tensor bootstrapping errors largely increase with distance compared with two-tensor bootstrapping errors

after the tracts enter crossing regions (Region 1 ,2, and 3) in all cases, because single-tensor fibre tracts diverge in the wrong direction (Fig.3A,C and D) in these regions.

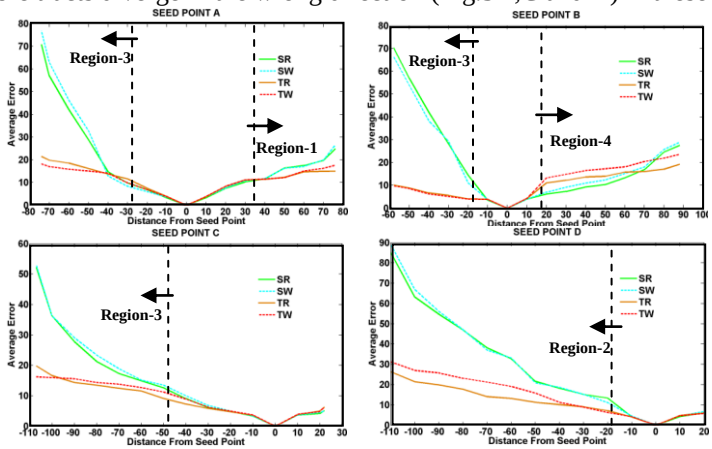

Fig. 4. Comparison of the four probabilistic tracking algorithms (single-tensor residual (SR) and wild (SW) and two-tensor residual (TR) and wild (TW)) from four seed points A, B,C and D with the average error (in mm) at different distances from the seed point.

***In vivo* Data:** Figs 5-7 show individual probabilistic fiber trajectories in the region with complex fiber architecture. The seed points were placed at the centre of three well known fibre tracts; the CC, the SLF and the CST and all five tractography methods (Single-tensor residual (a) and wild (b) and two-tensor residual (c), wild (d) and repetition (e)) were initiated from these seed points.

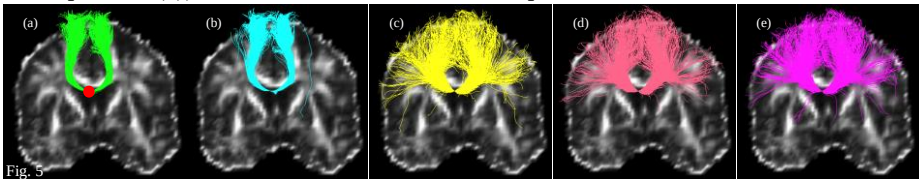

Fig. 5 shows that the five bootstrap tractography methods are able to reconstruct the CC. Two-tensor bootstrap fibre tracking techniques were able to more accurately delineate the callosal radiation than single-tensor bootstrap tractography. The two-tensor model-based bootstrap tractography methods were able to traverse the regions of crossing fibres and connectivity observed throughout the lateral frontal and parietal lobes while single-tensor tracts only showed connectivity between the left and right superior frontal gyri of both hemispheres.

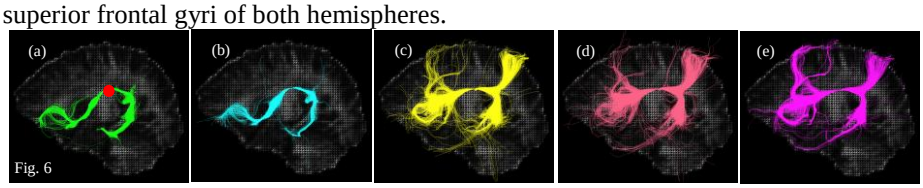

Fig. 6 shows that two-tensor bootstraps are able to reconstruct a well defined tract through the SLF. Two-tensor bootstrap tractography shows more white matter connections passing through the seed point, demonstrating not only central parts of the SLF, but also fibres reaching more distally and links and projections to parts of

the inferior longitudinal fascicle, cingulum and links between subcortical areas with a much higher degree of dispersion, not observed in both single-tensor cases.

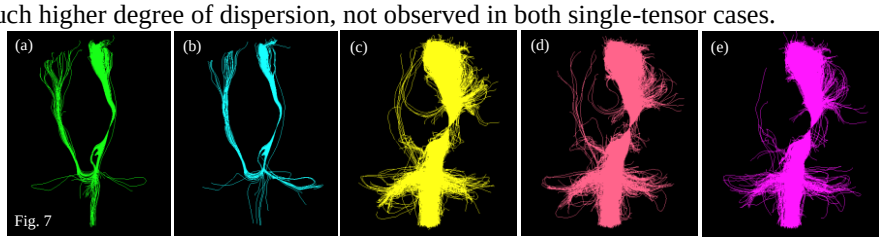

Fig. 7

Fig. 7 shows that bootstrap tractography is able to reconstruct the CST from the cortex to the spinal cord from a seed point placed in the internal capsule. Both single-tensor results indicate that a number of streamlines erroneously cross and project into the contralateral hemisphere. Looking at the two-tensor tractography results there is generally a much higher degree of dispersion. Two-tensor residual, wild and repetition bootstrap produced very similar reconstructions of all three tracts and higher fibre dispersion values were observed compared to single-tensor bootstrapping results, especially as the tracts move further from the seed point.

In summary, based on our experimental evaluations, the advantages of the proposed two-tensor model-based bootstrap algorithms are threefold. First, we can use data which is routinely available from clinical scans to implement this approach and unlike previous bootstrap methods with other multi-fibre modalities our algorithms show improved computational efficiency, making them clinically feasible. Secondly, our bootstrap algorithms are implemented on appropriate tensor morphology voxels to increase the validity of the probabilistic bootstrap distribution. Thirdly, our algorithms can accurately reconstruct fibre paths and are also able to recover complex fibre configurations.

References

1. Pajevic, S., Basser, P.J.: Parametric and non-parametric statistical analysis of DT-MRI data. J. Magn. Reson., 161, 1–14 (2003)
2. Whitcher, B., Tuch, D. S., Wisco, J. J., Sorensen, A. G., Wang, L.: Using the wild bootstrap to quantify uncertainty in diffusion tensor imaging. Hum. Bra. Map., 29, 346–362 (2008)
3. Chung, S., Lu, Y., Henry, R.G.: Comparison of bootstrap approaches for estimation of uncertainties of DTI parameters. NeuroImage, 33, 531–541 (2006)
4. Yuan, Y., Zhu, HT., Ibrahim, JG., Peterson, B., Lin, W.L.: A note on the validity of statistical bootstrapping for estimating the uncertainty of tensor parameters in diffusion tensor images. IEEE Trans Med Imaging, 27, 1506-1514 (2008)
5. Tuch, D., Reese, T., Wiegell, M., Makris, N., Belliveau, J., Wedeen, V.: HARDI reveals intravoxel white matter fiber heterogeneity. Magn. Reson. Med., 48 (4), 577–582 (2002)
6. Tuch, D.S.: Q-ball imaging. Magn Reson Med, 52, 1358–1372 (2004)
7. J. D. Tournier, F. Calamante, and A. Connelly. Robust determination of the fibre orientation distribution in diffusion MRI: non-negativity constrained super-resolved spherical deconvolution. Neuroimage, 35, 1459–72 (2007)
8. Peled, S., Friman, O., Jolesz, F.,Westin, C.F.: Geometrically constrained two-tensor model for crossing tracts in DWI. Magn. Reson. Imaging, 24, 1263–1270 (2006)
9. Zhu, H. T., Xu, D., Amir, R., Hao, X., Zhang, H., Alayar, K., Ravi, B., Peterson, B.: A statistical framework for the classification of tensor morphologies in diffusion tensor images. Magn. Reson. Imag., 24, 569–582 (2006)
10. Westin, C.F., Maier, S.E., Mamata, H., Nabavi, A., Jolesz, F.A., Kikinis, R.: Processing and visualization for diffusion tensor MRI. Med. Image Anal., 6, 93–108 (2002)